Using limited neural networks to assess relative mechanistic influence on shock heating in granular solids

Brenden W. Hamilton* and Timothy C. Germann
Theoretical Division, Los Alamos National Laboratory, Los Alamos, New Mexico 87545, USA

(Received 16 May 2023; accepted 1 August 2023; published 14 August 2023)

The rapid compaction of granular media results in localized heating that can induce chemical reactions, phase transformations, and melting. However, there are numerous mechanisms in play that can be dependent on a variety of microstructural features. Machine learning techniques such as neural networks offer a ubiquitous method to develop models for physical processes. Limiting what kind of microstructural information is used as an input and assessing normalized changes in network error, the relative importance of different mechanisms can be inferred. Here we utilize binned, initial density information as network inputs to predict local shock heating in a granular high explosive trained from large-scale molecular dynamics simulations. The spatial extent of the density field used in the network is altered to assess the importance and relevant length scales of the physical mechanisms in play, where different microstructural features result in different predictive capabilities.

DOI: 10.1103/PhysRevMaterials.7.085601

I. INTRODUCTION

The rapid compaction of granular solids can lead to a wide variety of microstructural [1–4] and chemical [5–8] responses that are highly dictated by the initial local packing and structure of the material. While the use of molecular dynamics (MD) and continuum mechanics simulations have helped to elucidate the governing processes [9–16], the wide range of mechanisms in play have prevented a unified understanding of events, especially the weighted relevance of various mechanisms.

A key example is the shock compression of energetic materials, which are typically neat or polymer-bonded granular solids with a bimodal grain size distribution of larger grains and smaller "fills" [17–19]. The shock initiation of chemistry, which can lead to a run to detonation, is governed by the formation of localizations of excess energy known as hotspots, which are typically defined by their temperature and size [20,21]. These hotspots form through shock-induced processes such as intra- and intergranular void collapse, shear band formation, jetting of material, and intergranular friction [22–26]. From system to system, these individual processes can be influenced by material orientations, crystal defect formation, surface properties, and void shapes and sizes [27–34]. Void collapse is typically the dominant process, with the energy localization increasing with increasing pressure-volume (P-V) work done [35]. Additionally, the range of grain sizes utilized greatly affects the shock initiation and detonation processes for nanometer- and micrometer-scale grains [36,37]. Hence broadly understanding the overall shock compression and initiation involves a wide range of materials models and highly detailed structural information.

Additionally, shock compaction not only localizes thermal energy, but also can deform individual molecules, causing them to exist in strained states [38]. These intramolecular strains can alter reaction kinetics and pathways through mechanochemistry [39–41]. Interestingly, these strain energies are thought to occur through fundamentally different processes than temperature localization [33,42]. Being able to predict the localization of both temperature and strain energy in a hotspot remains a grand challenge for the energetic materials community and is highly relevant to general materials compaction problems. Being able to predict these processes without running computationally expensive molecular dynamics and hydrocode simulations, as well as to better evaluate the key or necessary mechanisms, is crucial to the materials physics and condensed matter chemistry communities.

Materials science, in general, has recently experienced a rapid increase in the use of machine learning (ML) to extract and understand physical processes that can occur [43–45]. ML has played a key role in the development of computational models [46–52], predicting properties [53–57], and characterizing materials [58–61]. While predictions from large and nonlinear neural networks typically function as a black box, limiting and altering the physical information that informs the network can help to tease out which properties and mechanisms are critical to a process by the network's ability to make predictions given its limited subset of input information. This process, employed here, is similar to a "leave one feature out" scheme.

Here, we utilize nonreactive, all-atom MD simulations to model the shock response of the granular high explosive 1,3,5-triamino-2,4,6-trinitrobenzene (TATB). A neural network is used to predict the final temperature and intramolecular strain energy fields, given just the initial density field of the unshocked system. The level of coarsening and total extent of the density information given are varied to assess the amount of local information needed to properly predict energy localization from granular compaction. Increasing density resolution provides more information pertaining to pore shape and local

*brenden@lanl.gov

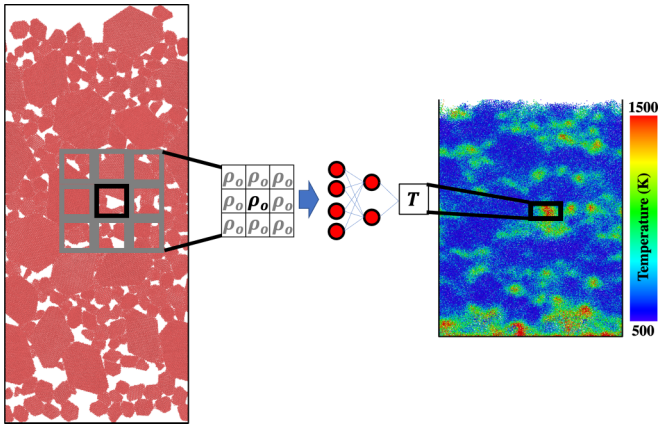

FIG. 1. Initial configuration and composite temperature map for the testing set system with example binning for network input and output.

curvature, but using only density restricts potentially critical information such as local crystal orientation and crystalline defects. It should be noted that the purpose of this work is not to minimize the error of the networks and make the best model possible. It is to systematically change the inputs given to the network such that physical trends and important physicochemical mechanisms can be inferred from the relative change in each network's predictive ability. However, this methodology does necessitate that the network predictions be reasonably accurate as a baseline for extracting materials physics, such that the model is presumably learning some description of the physics.

II. METHODS

A. Molecular dynamics

All simulations were run with all-atom MD using the Large-Scale Atomic/Molecular Massively Parallel Simulator (LAMMPS) software package [62,63]. Interatomic interactions were calculated using the nonreactive, nonpolarizable force field from Bedrov *et al.* [64], with tailored harmonic bond stretch and angle bend terms [65] and an intramolecular O-H repulsion term [66]. Electrostatics were solved for in real space with the Wolf potential [67]. The van der Waals interactions were modeled using the Buckingham potential. All simulations are conducted with a 0.25 fs time step.

Simulation cells of granular TATB were built with the PBXGen algorithm [17] using columnar (periodic and no change in shape into the page) grains with a bimodal grain size distribution with peaks at 40 and 8 nm. The smaller "fill" grains make up roughly 2/3 of the total grain count. All grains are crystallographically oriented so that the TATB [001] direction is in the periodic Z direction with a thickness of 4.1 nm (into the page in Figs. 1 and 3), which minimizes grain-to-grain anisotropy. Within the plane, the grains are randomly rotated. Two cells were constructed with different sizes: 100×400 nm (12 440 592 atoms) and 100×200 nm (6 183 984 atoms), where the larger system is used to make up the training set and the smaller system is the testing set.

As PBXGen packed systems typically only have a volumetric packing density of around 50%, the initial cell sizes were 200×400 and 200×200 nm. The X direction was then compacted to the final size over a period of 250 ps. The temperature was set 500 K to promote grain boundary formation and to help anneal defects formed during compaction. The atom coordinates were fractionally remapped at every step during compaction. The final cells were thermalized at 300 K for 25 ps.

Shock simulations were conducted using the reverse ballistic method with a particle velocity of 2.0 km/s, with the resulting shock traveling in the $+Y$ direction (upwards in Figs. 1 and 3). This was performed by adding the negative of the particle velocity to all atoms in the system with a perfectly reflecting momentum mirror at the bottom boundary in the shocked direction [68]. This resulted in the shocked material being stationary, which is preferable for analysis, and is identical to using a moving piston into stationary material via Galilean invariance. The Y direction was a free boundary, whereas the other directions were periodic. Analysis was conducted using a per molecule basis, using the molecular center of mass (c.m.) as its position. Temperature T was the molecular rotovibrational kinetic energy in units of kelvin, calculated with a classical specific heat. From the per atom velocities, we computed three kinetic energy values: total, translational, and rotovibrational.

$$\mathrm{KE_{tot}} = \sum \frac{1}{2} m_i (v_i \cdot v_i), \tag{1}$$

$$\mathrm{KE_{trans}} = \frac{1}{2} M (V \cdot V), \tag{2}$$

$$\mathrm{KE_{ro\text{-}vib}} = \mathrm{KE_{tot}} - \mathrm{KE_{trans}}, \tag{3}$$

$$\mathrm{KE_{ro\text{-}vib}} = \frac{3N_a - 3}{2} k_B T, \tag{4}$$

where we define c.m. properties with capital letters and atomic properties with lowercase letters. M and m correspond to mass, V and v are velocity, k_b is Boltzmann's constant, and N_a is the number of atoms per molecule. Variables with subscript i were indexed from 1 to N_a. Intramolecular strain energy U_{latent} was defined as the excess intramolecular potential energy U_{intra} with respect to the equipartition theorem [28]:

$$U_{\mathrm{intra}} = \sum U_{\mathrm{bond}} + \sum U_{\mathrm{ang}} + \sum U_{\mathrm{dih}} + \sum U_{\mathrm{imp}}, \tag{5}$$

$$U_{\mathrm{latent}} = U_{\mathrm{intra}} - \mathrm{KE_{ro\text{-}vib}}. \tag{6}$$

B. Machine learning

For the neural networks, a sigmoid function is used into the hidden layer, and a linear function into the output layer. A bias is allowed for both layers. All networks have a single hidden layer. Predictions of temperature (T) and intramolecular strain energy (U_{latent}) fields are done with separate networks.

The system is binned in a Lagrangian fashion on the initial frame prior to shock compression in order to provide the density descriptors. While the Lagrangian scheme negates the bin-to-bin mass flow issues of an Eulerian scheme, we do assume that changes to bin size and shape are learned by the network as part of the shock heating mechanisms, which may contribute to a portion of the error here. From the

simulation, each molecule has a defined time it is "shocked" based on large local changes in c.m. velocity. A "composite frame" of the shocked state is constructed by taking the position and thermodynamics at each molecule at 5 ps after its shocked time, i.e., molecules are taken from different simulation frames such that they are at the same relative time compared with their time of being compressed. The composite frame is used for the network outputs to minimize effects from various dissipation mechanisms as the compression processes are in spatial nonequilibrium.

The input layer consists of the density of a bin and its N sets of nearest neighbors (initial frame), as shown in Fig. 1 for the $N = 1$ case (a second shell of bins would be $N = 2$, and just the central bin, no neighbors, is $N = 0$). Bins with zero molecules are considered as neighbor bins but not as center bins as they will not have a final temperature or energy for an output. The output layer is either the T or U_{latent} of the center bin (composite frame); each of these two values is trained with separate networks of the same architecture.

All networks consist of an input layer of size $(2N + 1)^2$, an output layer of size 1, and a single hidden layer of size $\lfloor 0.5(2N + 1)^2 \rfloor$. For $N = 0$, the hidden layer is size 1. Figure 1 exemplifies how the all-atom structure is encoded into the neural network input layer, where the output layer corresponds to a region of the all-atom results, the same center Lagrangian bin, which has mean T and U_{latent} values.

Different square bin sizes of 2.5, 3.0, 4.0, and 5.0 nm are used. To compare different bin size results, we define the spatial extent (SE) of the input layer: $\text{SE} = L(N + \frac{1}{2})$, where L is the bin length and N is the number of sets of nearest-neighbor bins included. This is the equivalent to the radius of an inscribed circle for the total square of bins used.

An 80-20 split is used during training. An early stopping criterion is set to stop training and take the best network if the mean-square error of the 20% testing group does not drop by at least 0.000 01 over 100 epochs. This error delta is in normalized units, where all input and output data are utilized as the Z score of the data. An Adam optimizer is used with a 1×10^{-3} learning rate. All error values presented in this paper are based on predictions of the smaller of the MD systems which is not included in training at all. Within the input layer for a given network, the order of the bins is constant in the input layer, such that the network can differentiate upstream and downstream of the bin, as well as some information regarding the shape of a pore.

III. RESULTS AND DISCUSSION

Figure 2 shows parity plots of T and U_{latent} for $L = 5.0$ and 2.5 nm, with nearly equivalent spatial extents of 27.5 and 26.25 nm, respectively. For the temperature (left column plots), both show decent correlation with the parity line, with root-mean-square (RMS) errors of 84.4 and 108.9 K for the 5.0- and 2.5-nm bins, respectively, where peak (individual) molecular temperatures in the hotspots are over 1500 K and are 600–700 K in the bulk shocked materials. Certain high-temperature points are overpredicted while others are underpredicted, alluding to some microstructural influence in which some critical descriptors may not be captured by the density field.

When comparing the two sets at different bin sizes, it is crucial to consider that while using the 2.5-nm bins results in four times as many training and testing points, it also samples a much wider range of values, as the smaller bins provide less smoothing of extreme temperatures. The 2.5-nm case has considerably more values above 1000 K, and its peak hotspot temperatures are much higher than the bulk temperature, relative to the 5.0-nm bins. The smaller-bin case must also predict more local gradients which includes a range of hotspot temperatures, whereas in the 5-nm case, many hotspots are captured within a single bin and therefore have a single temperature value.

For the U_{latent} predictions shown in Fig. 2, there is considerably less correlation with the parity line. The predictions even appear to be less correlated overall at the smaller bin sizes. While the U_{latent} fields, shown in Sec. SII of the Supplemental Material [69], are more disperse than the T fields, there are still notable regions of higher and lower strain energy. The predicted fields are considerably more homogeneous and noisy, showing that the density field alone is not enough to predict the mechanisms that drive molecules to bent and distorted shapes, and that more complicated microstructural or thermodynamic information is likely needed to make these predictions. This additionally helps to verify previous results that concluded that the T and U_{latent} forming mechanisms are different, as their localizations do not occur on a one-to-one basis [38]. U_{latent} also has a strong influence from pore size at larger pores [33], and the system sizes here may not be large enough to provide a wide enough range of examples in the training set. Compared with temperature, the density (and therefore P-V work) alone is not enough to make decent quantitative predictions of the U_{latent} field.

Figure 3 shows heat maps of the actual and predicted temperatures, as well as the difference, for the 2.5-nm-bin case. Other bin-size and nearest-neighbor cases are available in Sec. SI of the Supplemental Material [69]. From this, it can be assessed that hotspots that are longer in the shock direction, such as points a and b in Fig. 3, are underpredicted. However, hotspots that are longer in the cross direction, such as points c and d in Fig. 3, are overpredicted. The initial microstructure of this case is shown in Fig. 1. Vertical pores and high aspect curvature pores can often result in molecular jetting, leading to high levels of expansion before getting recompressed [23,31,70]; however, wider or more circular pores often result in more hydrodynamic or plastic-flow-type responses that incur much less P-V work during recompression relative to the jetted material, especially as material will have less physical space to expand into the pore before getting recompressed. It should be noted that while there are underpredictions of the hottest hotspots and overprediction of the colder ones, the model still generally predicts vertical pores to be hotter than the horizontal ones.

The two key factors in qualitatively predicting hotspot temperatures from pore collapse are the pore size and shape [9,23,33]. Based on these results, the predictions here appear to be fully considering size, with the largest pores (points a and c) predicting high temperatures and the smaller pores typically predicting lower temperatures. Molecular jetting, which greatly influences material expansion into pores, is a much more complex mechanical process where things

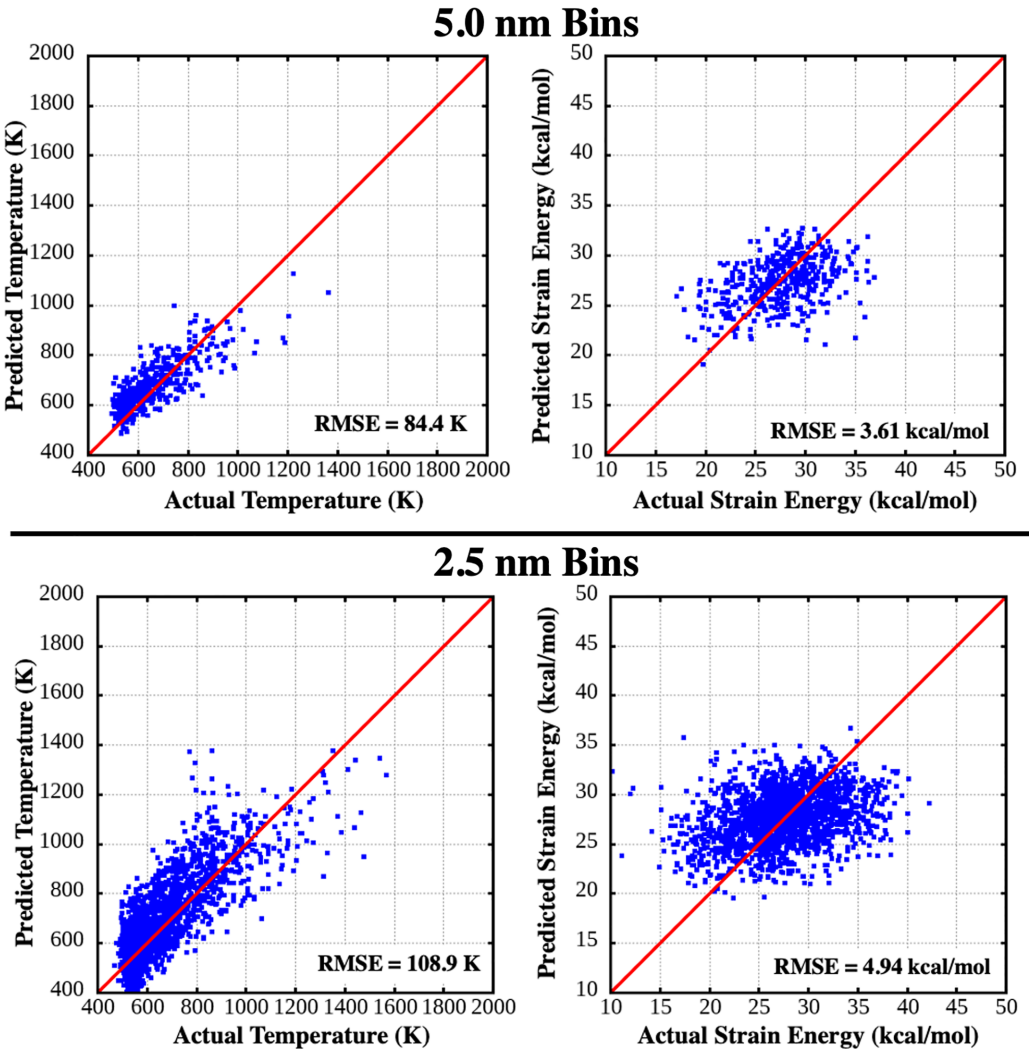

FIG. 2. Parity plots of T and U_{latent} for the 5.0-nm bins and 2.5-nm bins for spatial extents of 27.5 and 26.25 nm, respectively. Data consist of predictions of the smaller MD cell used exclusively for testing.

such as curvature of the pore come into play [23,31]. Even with small initial bins, this information is partially coarsened out, preventing the network from making these predictions. Information on the shock wave structure and shape, which will change as it progresses over the material, is also unknown to the network and can cause different amounts of shock focusing that leads to jetting. Additionally, the network does not have information related to crystal orientation, which results in changes in hotspot temperature on the order of the errors shown here [28]; however, the grain orientations chosen here minimize anisotropy between grains. Hence, while P-V work from pore size is enough to make decently quantitative predictions of hotspot temperature, the finer microstructural details are likely needed to correct for errors on the order of several hundred kelvin. It is most likely a combination of these omitted features that drives the error in predictions, especially the underprediction of the highest-temperature hotspots.

Figure 4 shows root-mean-square (RMS) errors and linear normalized RMS errors (LN-RMSEs) for all networks trained. The LN-RMSEs are RMSE values normalized by the RMSE of the linear regression between the density of a bin (no nearest-neighbor information) and the temperature, presented as the ratio of the nonlinear network RMSE and the linear network RMSE. In Fig. 4, which shows the error results for predictions of the temperature fields, we interestingly see, for small to intermediate spatial extent, similar RMSEs from all bin sizes, followed by a divergence of values. The slight uptick in errors for large spatial extent are attributed to a static stopping criteria based on error reduction over the previous 200 epochs. For larger SE, the network itself is proportionally larger and potentially learns at a slower rate, especially for smaller bin sizes where N is much larger for a given SE and the network size grows as N^2.

For an equal spatial extent between two different bin sizes, the smaller bin will result in more training or testing data for a given simulation size. However, the smaller-bin system is also less coarse grained and will have a wider range of peak temperatures and more pronounced temperature gradients. Hence, with more training data and more resolved microstructural data from the density input, the smaller bins are able to reach roughly the same level of predictive power as for the much smoother fields of the larger bins. For the LN-RMSE, as smaller bins will have more variability in temperature with density and therefore a larger normalizing constant, the

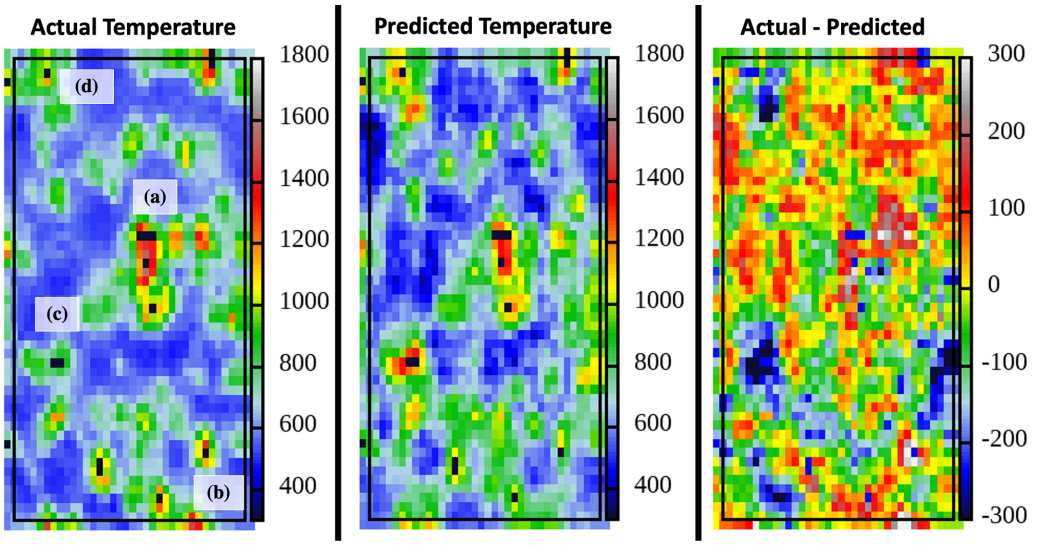

FIG. 3. Heat maps of the actual and predicted temperatures, as well as the difference between the two, for the 2.5-nm-bin case with a 26.25 nm spatial extent. Points a–d on the actual temperature map correspond to specific hotspots, where points a and b are underpredicted and points c and d are overpredicted.

smallest-bin cases perform the best. This normalized case shows the predictive power of adding more microstructural information with a finer density field. As there is significantly less accuracy in the U_{latent} predictions, the trends of decreasing errors with SE and various bin size effects are less physically meaningful. Plots of RMSE and LN-RMSE for U_{latent} are available in Sec. SIII of the Supplemental Material [69]. These show similar trends with SE to temperature, yet opposite trends with respect to bin size, which is most likely an effect of coarsening significant noise and the ease of predicting a more uniform field.

IV. CONCLUSIONS

In summary, MD simulations of shock compaction of a granular material resulted in heterogeneous localization of both temperature and intramolecular strain energy, where the latter is known to be responsible for mechanochemical effects. A Lagrangian binning of initial microstructures was used to embed local density information, but intentionally excludes information pertaining to local crystal structure, defects, orientation, and incident wave structure. These density bins were utilized as an input layer to a neural network to predict the shock induced T and U_{latent} fields.

From trends in RMS errors for different bin sizes and spatial extents of the input layer, we find that the predictability of a network increases with more spatial extent, as well as with smaller bins which would carry more precise microstructural information. These improvements are despite the smaller bins leading to much larger variability and fluctuation in the temperature fields, where larger bins smooth and coarsen that information.

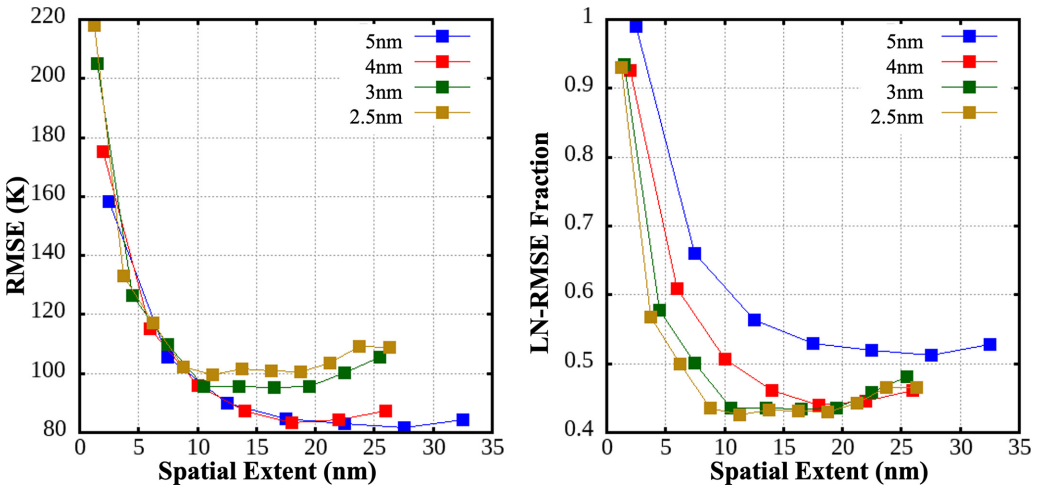

FIG. 4. Root-mean-square errors for all temperature networks run, as a function of spatial extent. Colored lines represent different bin sizes. LN-RMSEs (linear normalized RMSEs) are RMS errors that are normalized by the RMS error of a linear network for zero nearest neighbors ($N = 0$).

While density information did not allow for accurate prediction of U_{latent}, the networks readily predicted the temperature fields with some of the hotspots being overpredicted, while others are underpredicted. While the network predicts hotter temperatures for larger pores, where more *P-V* work can occur during compaction, it fails to fully capture other mechanisms such as jetting and molecular ejecta, which can lead to extreme temperatures. This failure manifests in pores that nucleate these jetting mechanisms, those elongated in the shock direction, to have underpredicted temperatures. Additionally, equiaxed or wider pores that do not jet are slightly overpredicted. This leads the network to give less variation in prediction from hotspot to hotspot, but still captures the general trend with pore size.

Hence we are able to utilize neural network predictions to show that while *P-V* work is the dominant mechanism in temperature localization, not having finer microstructural details such as those on the nanometer to subnanometer length scale leads to errors with the hotspot on the order of a few hundred kelvin. Additionally, *P-V* work and pore shape are shown to be much less important mechanisms for the U_{latent} field, which may have considerable influence from plasticity levels and material flow rate [25,33].

This work shows promise in the use of these limited neural networks to assess physical mechanisms in play for complex, physicochemical processes in condensed matter systems. In future work, a wider variety of input descriptors can be utilized that, in addition to density, map features such as crystal orientation, preexisting crystalline defects, surface roughness in pores, and the structure or shape of the incident shock wave which will be altered from upstream microstructural features and shock instabilities. By coupling these features with a "leave one feature out"-type scheme and the varying-spatial-extent scheme used here, the relative importance of key hotspot mechanisms and their necessary descriptors can be deduced.

In general, we believe the workflow developed here is widely applicable to a variety of materials' processes in granular systems that can be simulated or experimentally probed with high resolution in which to train a model. Measurable and mathematically describable packing of granular materials ranging from micrometer to millimeter scales [71], as well as simulatable systems down to the nanoscale [17], offers a route to design significantly larger training sets than used here which would span multiple orders of magnitude and time and length scale processes. Having good structural characterizations of these packings [72], as shown here, is crucial to accurately modeling dynamic processes in these materials. Significant future work is needed to extend the ideas here to be valid for loose packings in large systems in which the length scales of microstructural features can vary by many orders of magnitude [71,72].

ACKNOWLEDGMENTS

Funding for this project was provided by the Director's Postdoctoral Fellowship program at Los Alamos National Laboratory, LDRD Project No. 20220705PRD1. Partial funding was provided by the Advanced Simulation and Computing Physics and Engineering Models project (ASC-PEM). This research used resources provided by the Los Alamos National Laboratory (LANL) Institutional Computing Program. This work was supported by the U.S. Department of Energy (DOE) through LANL, which is operated by Triad National Security, LLC, for the National Nuclear Security Administration of the U.S. Department of Energy (Contract No. 89233218CNA000001). Approved for Unlimited Release LA-UR-23-24466.

[1] M. J. Cherukara, T. C. Germann, E. M. Kober, and A. Strachan, Shock loading of granular Ni/Al composites. Part 1: Mechanics of loading, J. Phys. Chem. C **118**, 26377 (2014).

[2] J. Brujić, P. Wang, C. Song, D. L. Johnson, O. Sindt, and H. A. Makse, Granular Dynamics in Compaction and Stress Relaxation, Phys. Rev. Lett. **95**, 128001 (2005).

[3] G. Lumay and N. Vandewalle, Experimental Study of Granular Compaction Dynamics at Different Scales: Grain Mobility, Hexagonal Domains, and Packing Fraction, Phys. Rev. Lett. **95**, 028002 (2005).

[4] V. Busignies, P. Tchoreloff, B. Leclerc, C. Hersen, G. Keller, and G. Couarraze, Compaction of crystallographic forms of pharmaceutical granular lactoses. II. Compacts mechanical properties, Eur. J. Pharm. Biopharm. **58**, 577 (2004).

[5] M. J. Cherukara, T. C. Germann, E. M. Kober, and A. Strachan, Shock loading of granular Ni/Al composites. Part 2: Shock-induced chemistry, J. Phys. Chem. C **120**, 6804 (2016).

[6] A. Strachan, A. C. van Duin, D. Chakraborty, S. Dasgupta, and W. A. Goddard, Shock Waves in High-Energy Materials: The Initial Chemical Events in Nitramine RDX, Phys. Rev. Lett. **91**, 098301 (2003).

[7] Y. Yang, R. Gould, Y. Horie, and K. Iyer, Shock-induced chemical reactions in a Ni/Al powder mixture, Appl. Phys. Lett. **70**, 3365 (1997).

[8] X. Zhou, Y. R. Miao, W. L. Shaw, K. S. Suslick, and D. D. Dlott, Shock wave energy absorption in metal-organic framework, J. Am. Chem. Soc. **141**, 2220 (2019).

[9] M. A. Wood, D. E. Kittell, C. D. Yarrington, and A. P. Thompson, Multiscale modeling of shock wave localization in porous energetic material, Phys. Rev. B **97**, 014109 (2018).

[10] S. D. Herring, T. C. Germann, and N. Grønbech-Jensen, Effects of void size, density, and arrangement on deflagration and detonation sensitivity of a reactive empirical bond order high explosive, Phys. Rev. B **82**, 214108 (2010).

[11] N. K. Rai, O. Sen, and H. S. Udaykumar, Macro-scale sensitivity through meso-scale hotspot dynamics in porous energetic materials: Comparing the shock response of 1,3,5-triamino-2,4,6-trinitrobenzene (TATB) and 1,3,5,7-tetranitro-1,3,5,7-tetrazoctane (HMX), J. Appl. Phys. **128**, 085903 (2020).

[12] X. Bidault and N. Pineau, Granularity impact on hotspot formation and local chemistry in shocked nanostructured RDX, J. Chem. Phys. **149**, 224703 (2018).

[13] Y. Xiong, X. Li, S. Xiao, H. Deng, B. Huang, W. Zhu, and W. Hu, Molecular dynamics simulations of shock loading of nearly fully dense granular Ni-Al composites, Phys. Chem. Chem. Phys. **21**, 20252 (2019).

[14] O. Pouliquen, M. Belzons, and M. Nicolas, Fluctuating Particle Motion during Shear Induced Granular Compaction, Phys. Rev. Lett. **91**, 014301 (2003).

[15] K. Kadau, T. C. Germann, P. S. Lomdahl, R. C. Albers, J. S. Wark, A. Higginbotham, and B. L. Holian, Shock Waves in Polycrystalline Iron, Phys. Rev. Lett. **98**, 135701 (2007).

[16] M. E. Rutherford, D. J. Chapman, J. G. Derrick, J. R. Patten, P. A. Bland, A. Rack, G. S. Collins, and D. E. Eakins, Probing the early stages of shock-induced chondritic meteorite formation at the mesoscale, Sci. Rep. **7**, 1 (2017).

[17] C. Li, B. W. Hamilton, T. Shen, L. Alzate, and A. Strachan, Systematic builder for all-atom simulations of plastically bonded explosives, Propellants, Explos., Pyrotech. **47**, e202200003 (2022).

[18] C. B. Skidmore, D. S. Phililips, P. M. Howe, J. T. Mang, and J. A. Romero, The evolution of microstructural changes in pressed HMX explosives (No. LA-UR-98-3473; CONF-980803-), Los Alamos National Lab.(LANL), Los Alamos, NM (United States, 1998).

[19] T. M. Willey, T. Van Buuren, J. R. Lee, G. E. Overturf, J. H. Kinney, J. Handly, B. L. Weeks, and J. Ilavsky, Changes in pore size distribution upon thermal cycling of TATB-based explosives measured by ultra-small angle X-ray scattering, Propellants, Explos., Pyrotech. **31**, 466 (2006).

[20] B. W. Hamilton, M. N. Sakano, C. Li, and A. Strachan, Chemistry under shock conditions, Annu. Rev. Mater. Res. **51**, 101 (2021).

[21] C. A. Handley, B. D. Lambourn, N. J. Whitworth, H. R. James, and W. J. Belfield, Understanding the shock and detonation response of high explosives at the continuum and meso scales, Appl. Phys. Rev. **5**, 011303 (2018).

[22] W. C. Davis, High explosives: The interaction of chemistry and mechanics, Los Alamos Sci. **2**, 48 (1981).

[23] C. Li, B. W. Hamilton, and A. Strachan, Hotspot formation due to shock-induced pore collapse in 1,3,5,7-tetranitro-1,3,5,7-tetrazoctane (HMX): Role of pore shape and shock strength in collapse mechanism and temperature, J. Appl. Phys. **127**, 175902 (2020).

[24] M. J. Cawkwell, T. D. Sewell, L. Zheng, and D. L. Thompson, Shock-induced shear bands in an energetic molecular crystal: Application of shock-front absorbing boundary conditions to molecular dynamics simulations, Phys. Rev. B **78**, 014107 (2008).

[25] M. P. Kroonblawd and L. E. Fried, High Explosive Ignition through Chemically Activated Nanoscale Shear Bands, Phys. Rev. Lett. **124**, 206002 (2020).

[26] J. K. Dienes, Discussion of a statistical theory of fragmentation processes, Mech. Mater. **4**, 337 (1985).

[27] P. Zhao, S. Lee, T. Sewell, and H. S. Udaykumar, Tandem molecular dynamics and continuum studies of shock-induced pore collapse in TATB, Propellants, Explos., Pyrotech. **45**, 196 (2020).

[28] B. W. Hamilton, M. P. Kroonblawd, and A. Strachan, The potential energy hotspot: Effects from impact velocity, defect geometry, and crystallographic orientation, J. Phys. Chem. C **126**, 3743 (2022).

[29] P. Lafourcade, C. Denoual, and J. B. Maillet, Irreversible deformation mechanisms for 1,3,5-triamino-2,4,6-trinitrobenzene single crystal through molecular dynamics simulations, J. Phys. Chem. C **122**, 14954 (2018).

[30] N. Grilli and M. Koslowski, The effect of crystal orientation on shock loading of single crystal energetic materials, Comput. Mater. Sci. **155**, 235 (2018).

[31] C. Li and A. Strachan, Shock-induced collapse of porosity, mapping pore size and geometry, collapse mechanism, and hotspot temperature, J. Appl. Phys. **132**, 065901 (2022).

[32] X. Bidault and N. Pineau, Impact of surface energy on the shock properties of granular explosives, J. Chem. Phys. **148**, 034704 (2018).

[33] B. W. Hamilton and T. C. Germann, Energy localization efficiency in 1,3,5-trinitro-2,4,6-triaminobenzene pore collapse mechanisms, J. Appl. Phys. **133**, 035901 (2023).

[34] B. W. Hamilton and T. C. Germann, Influence of pore surface structure and contents on shock-induced collapse and energy localization, J. Phys. Chem. C **127**, 9887 (2023).

[35] B. L. Holian, T. C. Germann, J. B. Maillet, and C. T. White, Atomistic Mechanism for Hot Spot Initiation, Phys. Rev. Lett. **89**, 285501 (2002).

[36] J. Liu, W. Jiang, Q. Yang, J. Song, G.-Z. Hao, and F.-S. Li, Study of nano-nitramine explosives: Preparation, sensitivity and application, Def. Technol. **10**, 184 (2014).

[37] Y. Wang, X. Song, D. Song, C. An, J. Wang, and F. Li, Mechanism investigation for remarkable decreases in sensitivities from micron to nano nitroamine, Nanomater. Nanotechnol. **6**, 184798041666367 (2016).

[38] B. W. Hamilton, M. P. Kroonblawd, C. Li, and A. Strachan, A hotspot's better half: Non-equilibrium intra-molecular strain in shock physics, J. Phys. Chem. Lett. **12**, 2756 (2021).

[39] B. W. Hamilton, M. P. Kroonblawd, and A. Strachan, Extemporaneous mechanochemistry: Shockwave induced ultrafast chemical reactions due to intramolecular strain energy, J. Phys. Chem. Lett. **13**, 6657 (2022).

[40] B. W. Hamilton and A. Strachan, Many-body mechanochemistry: Intramolecular strain in condensed matter chemistry, Phys. Rev. Mater. **7**, 075601 (2023).

[41] B. W. Hamilton and T. C. Germann, Interplay of mechanochemistry and material processes in the graphite to diamond phase transformation, arXiv:2302.04684.

[42] B. W. Hamilton, M. P. Kroonblawd, J. Macatangay, H. K. Springer, and A. Strachan, Intergranular hotspots: A molecular dynamics study on the influence of compressive and shear work, J. Phys. Chem. C **127**, 9858 (2023).

[43] R. Iten, T. Metger, H. Wilming, L. Del Rio, and R. Renner, Discovering Physical Concepts with Neural Networks, Phys. Rev. Lett. **124**, 010508 (2020).

[44] K. T. Butler, D. W. Davies, H. Cartwright, O. Isayev, and A. Walsh, Machine learning for molecular and materials science, Nature (London) **559**, 547 (2018).

[45] X. Zhong, B. Gallagher, S. Liu, B. Kailkhura, A. Hiszpanski, and T. Han, Explainable machine learning in materials science, npj Comput. Mater. **8**, 204 (2022).

[46] T. D. Huan, R. Batra, J. Chapman, S. Krishnan, L. Chen, and R. Ramprasad, A universal strategy for the creation of machine

learning-based atomistic force fields, npj Comput. Mater. **3**, 37 (2017).

[47] H. Chan, M. J. Cherukara, B. Narayanan, T. D. Loeffler, C. Benmore, S. K. Gray, and S. K. Sankaranarayanan, Machine learning coarse grained models for water, Nat. Commun. **10**, 379 (2019).

[48] Y. Zuo, C. Chen, X. Li, Z. Deng, Y. Chen, J. Behler, G. Csányi, A. V. Shapeev, A. P. Thompson, M. A. Wood, and S. P. Ong, Performance and cost assessment of machine learning interatomic potentials, J. Phys. Chem. A **124**, 731 (2020).

[49] P. Yoo, M. Sakano, S. Desai, M. M. Islam, P. Liao, and A. Strachan, Neural network reactive force field for C, H, N, and O systems, npj Comput. Mater. **7**, 9 (2021).

[50] R. K. Lindsey, L. E. Fried, and N. Goldman, ChIMES: A force matched potential with explicit three-body interactions for molten carbon, J. Chem. Theory Comput. **13**, 6222 (2017).

[51] B. W. Hamilton, P. Yoo, M. N. Sakano, M. M. Islam, and A. Strachan, High-pressure and temperature neural network reactive force field for energetic materials, J. Chem. Phys. **158**, 144117 (2023).

[52] Y. Zhang, C. Hu, and B. Jiang, Embedded atom neural network potentials: Efficient and accurate machine learning with a physically inspired representation, J. Phys. Chem. Lett. **10**, 4962 (2019).

[53] M. Fernandez, P. G. Boyd, T. D. Daff, M. Z. Aghaji, and T. K. Woo, Rapid and accurate machine learning recognition of high performing metal organic frameworks for CO_2 capture, J. Phys. Chem. Lett. **5**, 3056 (2014).

[54] T. Xie and J. C. Grossman, Crystal Graph Convolutional Neural Networks for an Accurate and Interpretable Prediction of Material Properties, Phys. Rev. Lett. **120**, 145301 (2018).

[55] M. N. Sakano, A. Hamed, E. M. Kober, N. Grilli, B. W. Hamilton, M. M. Islam, M. Koslowski, and A. Strachan, Unsupervised learning-based multiscale model of thermochemistry in 1,3,5-trinitro-1,3,5-triazinane (RDX), J. Phys. Chem. A **124**, 9141 (2020).

[56] L. Ward, A. Agrawal, A. Choudhary, and C. Wolverton, A general-purpose machine learning framework for predicting properties of inorganic materials, npj Comput. Mater. **2**, 16028 (2016).

[57] Y. Zhuo, A. Mansouri Tehrani, and J. Brgoch, Predicting the band gaps of inorganic solids by machine learning, J. Phys. Chem. Lett. **9**, 1668 (2018).

[58] M. R. Carbone, M. Topsakal, D. Lu, and S. Yoo, Machine-Learning X-Ray Absorption Spectra to Quantitative Accuracy, Phys. Rev. Lett. **124**, 156401 (2020).

[59] J. Timoshenko, D. Lu, Y. Lin, and A. I. Frenkel, Supervised machine-learning-based determination of three-dimensional structure of metallic nanoparticles, J. Phys. Chem. Lett. **8**, 5091 (2017).

[60] Y. Yao, H. Chan, S. Sankaranarayanan, P. Balaprakash, R. J. Harder, and M. J. Cherukara, AutoPhaseNN: unsupervised physics-aware deep learning of 3D nanoscale Bragg coherent diffraction imaging, npj Comput. Mater. **8**, 124 (2022).

[61] W. Hu, S. Ye, Y. Zhang, T. Li, G. Zhang, Y. Luo, S. Mukamel, and J. Jiang, Machine learning protocol for surface-enhanced raman spectroscopy, J. Phys. Chem. Lett. **10**, 6026 (2019).

[62] S. Plimpton, Fast parallel algorithms for short-range molecular dynamics, J. Comput. Phys. **117**, 1 (1995).

[63] A. P. Thompson, H. M. Aktulga, R. Berger, D. S. Bolintineanu, W. M. Brown, P. S. Crozier, P. J. in 't Veld, A. Kohlmeyer, S. G. Moore, T. D. Nguyen, R. Shan, M. J. Stevens, J. Tranchida, C. Trott, and S. J. Plimpton, LAMMPS - a flexible simulation tool for particle-based materials modeling at the atomic, meso, and continuum scales, Comput. Phys. Commun. **271**, 108171 (2022).

[64] D. Bedrov, O. Borodin, G. D. Smith, T. D. Sewell, D. M. Dattelbaum, and L. L. Stevens, A molecular dynamics simulation study of crystalline 1,3,5-triamino-2,4,6-trinitrobenzene as a function of pressure and temperature, J. Chem. Phys. **131**, 224703 (2009).

[65] M. P. Kroonblawd and T. D. Sewell, Theoretical determination of anisotropic thermal conductivity for crystalline 1,3,5-triamino-2,4,6-trinitrobenzene (TATB), J. Chem. Phys. **139**, 074503 (2013).

[66] N. Mathew, T. D. Sewell, and D. L. Thompson, Anisotropy in surface-initiated melting of the triclinic molecular crystal 1,3,5-triamino-2,4,6-trinitrobenzene: A molecular dynamics study, J. Chem. Phys. **143**, 094706 (2015).

[67] D. Wolf, P. Keblinski, S. R. Phillpot, and J. Eggebrecht, Exact method for the simulation of Coulombic systems by spherically truncated, pairwise r^{-1} summation, J. Chem. Phys. **110**, 8254 (1999).

[68] B. L. Holian and G. K. Straub, Molecular Dynamics of Shock Waves in Three-Dimensional Solids: Transition from Nonsteady to Steady Waves in Perfect Crystals and Implications for the Rankine-Hugoniot Conditions, Phys. Rev. Lett. **43**, 1598 (1979).

[69] See Supplemental Material at http://link.aps.org/supplemental/10.1103/PhysRevMaterials.7.085601 for additional results and figures.

[70] T. C. Germann, B. L. Holian, P. S. Lomdahl, A. J. Heim, N. Grønbech-Jensen, and J.-B. Maillet, Molecular dynamics simulations of detonation in defective explosive crystals, in *Proceedings of the Twelfth International Detonation Symposium* (Office of Naval Research, Arlington, VA, 2002), pp. 711–717.

[71] J. Schmidt, E. J. Parteli, N. Uhlmann, N. Woerlein, K.-E. Wirth, T. Poeschel, and W. Peukert, Packings of micron-sized spherical particles–insights from bulk density determination, x-ray microtomography and discrete element simulations, Adv. Powder Technol. **31**, 2293 (2020).

[72] C. Wang, K. Dong, and A. Yu, Structural characterization of the packings of granular regular polygons, Phys. Rev. E **92**, 062203 (2015).